Astron. Astrophys. 347, 355–365 (1999)

ASTRONOMY AND ASTROPHYSICS

A wavelet analysis of active region oscillations

J. Ireland[1,2], **R.W. Walsh**[2], **R.A. Harrison**[3], **and E.R. Priest**[2]

[1] NASA Goddard Space Flight Center, Room G-1, Building 26, Mail Code 682.3, Greenbelt, Maryland 20771, USA
[2] School of Mathematical and Computational Sciences, University of St. Andrews, St. Andrews, KY16 9SS, UK
[3] Space Science Department, Rutherford Appleton Laboratory, Chilton, Didcot, Oxfordshire, OX11 0QX, UK

Received 24 February 1999 / Accepted 21 April 1999

Abstract. The wavelet transform is applied to the analysis of active region oscillations. The localised (in time) nature of the wavelet transform allows us to study both the duration of any statistically significant oscillations as well as their period. Time series arising from SOHO (Solar and Heliospheric Observatory) CDS-NIS (Coronal Diagnostic Spectrometer Normal Incidence Spectrometer) active region observations on 14th-15th November 1996 are used to demonstrate the applicability of wavelet methods. High cadence (approximately 14 seconds) observations were made in He I 584.33 Å ($\log T_e = 4.3$), O V 629.73 Å ($\log T_e = 5.3$), Mg IX 368.06 Å ($\log T_e = 6.0$), Fe XVI 360.76 Å ($\log T_e = 6.4$) provide detailed intensity information on the active region over a wide range of temperatures. The distribution of statistically significant periods found varies from line to line, as does their duration.

Key words: Sun: chromosphere – Sun: corona – Sun: oscillations – Sun: transition region – Sun: UV radiation

1. Introduction

One of the principal objectives of the SoHO mission is to shed more light on how the solar corona is heated. Many mechanisms have been suggested in the literature as candidates, and many reviews exist outlining them in some detail (for example, Narain & Ulmschneider 1990, Browning 1991, Hollweg 1990 and Zirker 1993). Following Narain & Ulmschneider (1990), heating mechanisms may be divided into two basic classes, AC and DC. AC mechanisms are defined as those mechanisms that can be associated with rapid photospheric footpoint motions. Into this class falls magnetohydrodynamic wave mechanisms, such as phase mixing (Heyvaerts & Priest 1983, Hood et al. 1997), resonant absorption (Ruderman & Goossens 1993, Wright and Rickard 1995) and magnetoacoustic waves (Porter et al. 1994a, Porter et al. 1994b, Roberts et al. 1984, Laing & Edwin 1995). Conversely, DC mechanisms are associated with slow motions, which lead to magnetic field dissipation. Into this class falls magnetic reconnection mechanisms - for example, nanoflares Parker (1988) and magnetohydrodynamic turbulence (Heyvaerts & Priest 1992). It is likely that both AC and DC processes are probably at work in the solar corona - SoHO's task is to determine which dominates in which situation. This paper looks for evidence of AC mechanisms via the detection of oscillations in the solar atmosphere.

Much effort has gone into creating wave heating mechanisms that can deposit energy in the solar atmosphere, in particular the corona. Much effort too has gone into detecting both the waves themselves and any consequent heating (for a short review with respect to the capabilities of SoHO, see Ireland 1996). Pure acoustic waves are unlikely to exist in an atmosphere as strongly magnetised as the solar atmosphere; they are likely to be equivalent to slow mode magnetoacoustic waves. Acoustic waves can be largely dismissed as coronal heating mechanisms. Firstly, any acoustic waves generated at the photosphere will steepen and form shocks at the transition region, and go no further (Narain & Ulmschneider 1990 and references within). Secondly, Edwin (1991) calculates that the upper limit to the acoustic wave flux of $10\mathrm{Wm}^{-2}$ compared to the energy flux density of $10^4\mathrm{Wm}^{-2}$ renders acoustic wave heating relatively unimportant.

Alfvén waves have received extensive attention in the literature in connection with coronal heating. Heyvaerts & Priest (1983) suggest that phase mixing of Alfvén waves may contribute to coronal heating. In this mechanism, an Alfvén velocity structured transverse to the direction of wave propagation generates small lengthscales that enable the weak coronal damping to remove energy from the wave. The Alfvén wave amplitude is predicted to exhibit an $\exp(-ct^3)$ (for some value of c) dependence in closed structures such as coronal loops. Ulrich (1996) finds magnetohydrodynamic oscillations in the Na D1 line with a periods in the 5 minute band, observed from Mount Wilson. These oscillations are consistent with the properties of outgoing Alfvén waves and carry an estimated energy flux on the order of 3×10^7 erg cm^{-2}s^{-1}, sufficient for active region requirements.

The resonant absorption of Alfvén waves in coronal structures (typically loops) has been studied in detail, and seems well established both theoretically (Ionson 1978, Kappraff & Tataronis 1977) and numerically (Poedts & Kerner 1992, Karpen et al. 1994, Wright & Rickard 1995). However, numerical (Davila 1987) and theoretical (Hollweg 1987) calculations sug-

Send offprint requests to: J. Ireland (ireland@esa.nascom.nasa.gov)

gest that the main energy deposition region (the resonant layer) maybe either much less than or on the order of 1000 km, which, at best, would place such an observation at the limit of CDS and SOHO-SUMER (Solar Ultraviolet Measurements of Emitted Radiation) spatial resolution. Note, however, that Koutchmy et al., (1983) presented observational evidence for existence of resonant absorption in loops but the energy observed was insufficient to account for the loops' radiative losses.

As was mentioned above, magnetoacoustic waves are likely to exist in the corona. Švestka (1994) attributes quasi-periodic X-ray brightenings of about 20 minutes to slow standing magnetoacoustic waves, described theoretically Roberts et al., (1984). Porter et al., (1994a) suggests that slow mode waves with periods less than 300s/100s could damp sufficiently quickly enough to balance radiative energy losses in quiet/active solar regions. Chapman et al., (1972) provides evidence for a 262s intensity oscillations in the EUV ($T \lesssim 10^6$ K) from OSO-7. Also, Tsubaki (1977) demonstrates line of sight Doppler velocity, and to a lesser extent, line width, oscillations with periods around 300s in Fe XIV 5303 Å Sacramento Peak Observatory data.

Clearly, the detection of oscillations is an important step in determining the presence or otherwise of wave heating mechanisms. A wavelet analysis allows one to look at time series in a number of ways that are useful for solar applications. Bocchialini & Baudin (1994) examine some chromospheric velocity oscillations for both frequency and duration of oscillation. Frick et. al (1997) analyse sunspot number for variations in the 11 year period, while Aschwanden et al., (1998) uses a wavelet approach to study power law type behaviour in the timescales present in hard x-ray solar flares.

In this study we apply a wavelet approach to active region observations taken with CDS. Sect. 2 describes a campaign designed to look for oscillations in the solar atmosphere. Sect. 3 outlines the data processing methods used to find the results described in Sect. 4, and Sect. 5 discusses the results of this study.

2. The St. Andrews/RAL loops campaign

The findings described below form part of a series of observations taken with CDS on 12th-15th November, 1996. Two observing sequences were used, EJECT_V3 (version 18) and LOOPS_3 (version 1). CDS sequences are defined by a 6–8 letter acronym, and we note them here for future reference. Each observing sequence can be seen as a self-contained 'unit of observation' that serves a particular purpose. EJECT_V3 was originally designed to look at the onset of coronal mass ejections. This sequence uses the normal incidence part of CDS (see Harrison et al. 1995) with the 4×240arcsec^2 slit to look at six lines (He I 584.33 Å ($\log T_e = 4.3$), O V 629.73 Å ($\log T_e = 5.3$), Mg IX 368.06 Å ($\log T_e = 6.0$), Fe XVI 360.76 Å ($\log T_e = 6.4$), Si X 347.4 Å ($\log T_e = 6.0$) and Si 10 X 356.04 Å ($\log T_e = 6.0$)) at sixty different solar positions consecutively four arcseconds apart, building up an image in each line of about 240×240arcsec^2.

The first four lines cover a wide spread of formation temperatures (from the chromosphere (He), through the transition region (O) and into the corona (Mg and Fe)) while the last two lines are primarily intended as a density diagnostic at $T_e = 10^6$K. EJECT_V3 covers an area of 4×4arcmin^2 in a short period of time (about 15 minutes) and was used in this campaign to take a snapshot of the region of interest before and after multiple runs of the higher cadence, smaller area LOOPS_3 study. The relation of LOOPS_3 to EJECT_V3 is shown in Fig. 1. The narrow rectangles represent the positions of the LOOPS_3 observations overlaid on top of the EJECT_V3 observations.

Table 1. EJECT_V3 observing sequence.

Instrument	CDS-NIS, 4×240arcsec^2 slit
Locations	60, at 4 arcsec steps, total area, 240×240arcsec^2
Duration	10s per location, 991s for complete sequence.
Lines	He I 584.33 Å, O V 629.73 Å, Mg IX 368.06 Å, Fe XVI 360.76 Å, Si X 347.4 Å, Si X 356.04 Å

Table 2. LOOPS_3 observing sequence.

Instrument	CDS-NIS, 4×240arcsec^2 slit
Locations	1, total area 4×120arcsec^2
Duration	10s per location, 707s for a complete sequence of 50 rasters.
Lines	He I 584.33 Å, Mg IX 368.06 Å, O V 629.73 Å, Fe XVI 360.76 Å

LOOPS_3 is also a normal incidence observing sequence, using the 4×240arcsec^2 slit, that was specifically designed for this campaign to look for rapid variations in active regions. It is designed to provide spectroscopic information (used for Doppler velocity and line broadening studies) in four lines, widely spaced in formation temperature, at high cadence. Only 120 arcseconds of data along the slit is returned in order to reduce the overall cadence time. It covers the first four EJECT_V3 lines, but instead of rastering over a large area of the Sun, LOOPS_3 sits at one particular solar position and takes one image approximately every 14 seconds. Hence the returned data is essentially one dimensional in space (the solar Y direction) and has a cadence of about 14 seconds. One complete LOOPS_3 sequence takes 50 of these images, giving a total duration of about 700 seconds. A summary description of LOOPS_3 and EJECT_V3 are given in Tables 1 and 2 respectively.

A typical run of the campaign involved running EJECT_V3 initially to provide an overall view of the target active region. Then LOOPS_3 is run three times on one specific point of interest in that region, say at suspected coronal loop footpoints. Since the three LOOPS_3 studies are run consecutively with the same pointing, together they form a time series three times as long as one LOOPS_3 study.

To close the campaign, EJECT_V3 is run again to determine if any overall changes in the region of interest have occurred while LOOPS_3 has been running. The time series study presented below looks for oscillations with a sample time of about 14 seconds in time intervals of about 2100 seconds.

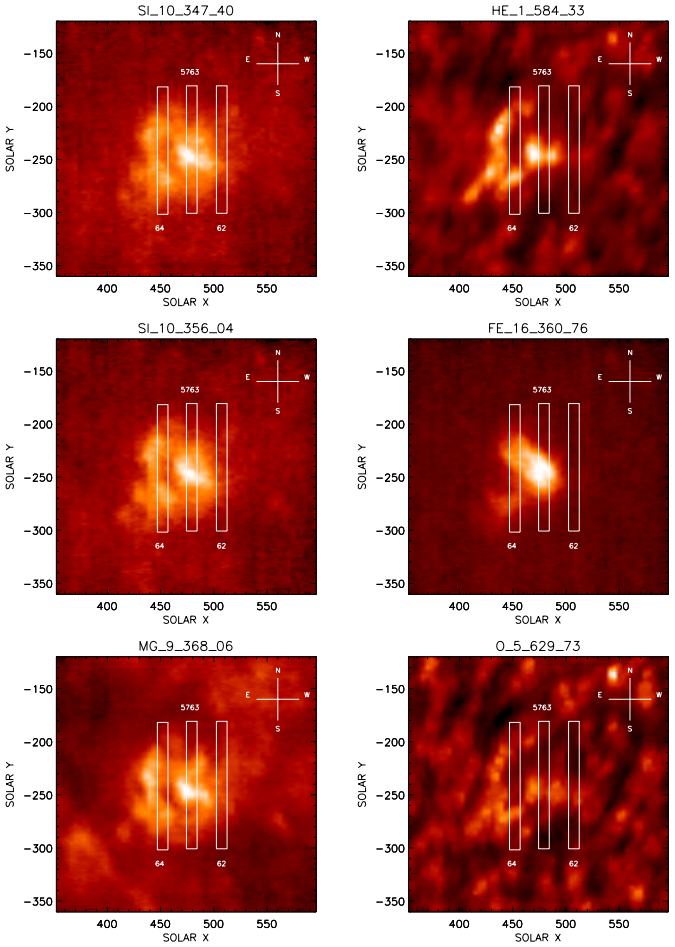

Fig. 1. Position of the observing slit for the three LOOPS_3 runs s5762, 63 and 64 respectively overlying EJECT_V3 data. Axes are in arcseconds.

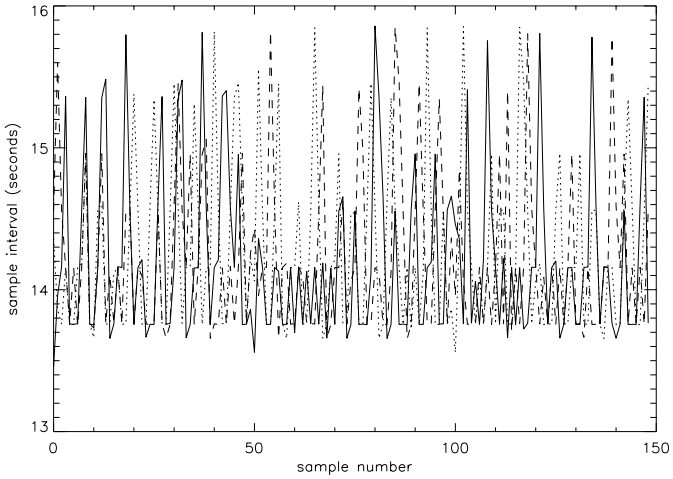

Fig. 2. Plot showing consecutive sample times for observing runs s5762 (solid line), s5763 (dashed line) and s5764 (dotted line).

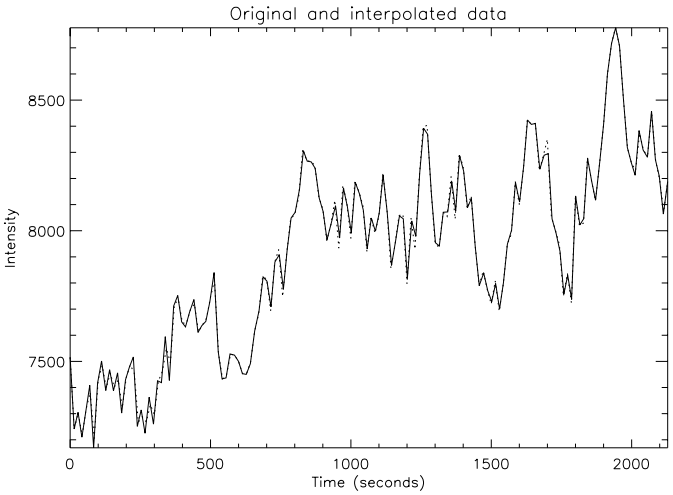

Fig. 3. Original (solid line) and interpolated (dotted line) time series.

3. Time series analysis

3.1. Preparation of the data

The data for each block of LOOPS_3 observations was first cleaned for cosmic ray hits on the detectors. These are easily identified as pixel enhancements or tracks. The CDS software package VDS_CALIB was run to convert the raw data into photon-events/pixel/second. Multiplying by the exposure time yields the photon-events per pixel. By concatenating the data in each LOOPS_3 block of observations, we form an observing run about 2100 seconds long. We shall look at time series formed by intensity variations only. The intensity of the line at each point is found by fitting a peak amplitude A, a position c, a line width w and coefficients a_0 and a_1 to the model

$$F(x) = A \exp\left[-\frac{1}{2}\left(\frac{x-c}{w}\right)^2\right] + a_0 + a_1 x \qquad (1)$$

i.e., one Gaussian plus a linear background to every solar Y position (solar Y is taken as the north-south direction along the slit, the first pixel being the northernmost) at every observation time. The total number of counts in the fitted Gaussian is taken as the total intensity I of the line. Of equal importance is the error in the total line intensity. Thompson (1998) describes a procedure for estimating this error in CDS-NIS data. The error σ_I^2 in the total line intensity consists of two parts;

$$\sigma_I^2 = \sigma_{\rm renorm}^2 + (f_N S)^2 \qquad (2)$$

The first error $\sigma_{\rm renorm}^2$ is due to the error in fitting the peak amplitude A and line width w. On fitting, errors σ_A^2 and σ_w^2 in peak intensity and line width respectively are calculated, as is the value of χ^2 for the fit. To get a better estimate of these errors, they are renormalized by multiplying by $\sqrt{\chi^2}$. Following Thompson (1998), we get

$$\frac{\sigma_{\rm renorm}^2}{I} = \frac{1}{2}\left[\frac{\sigma_A^2}{A} + \frac{\sigma_w^2}{w}\right] \qquad (3)$$

where σ_A^2 and σ_w^2 now refer to the renormalized values of the errors.

The second contribution arises from the photon statistics in CDS-NIS, and is due to two effects. The first is the Poisson

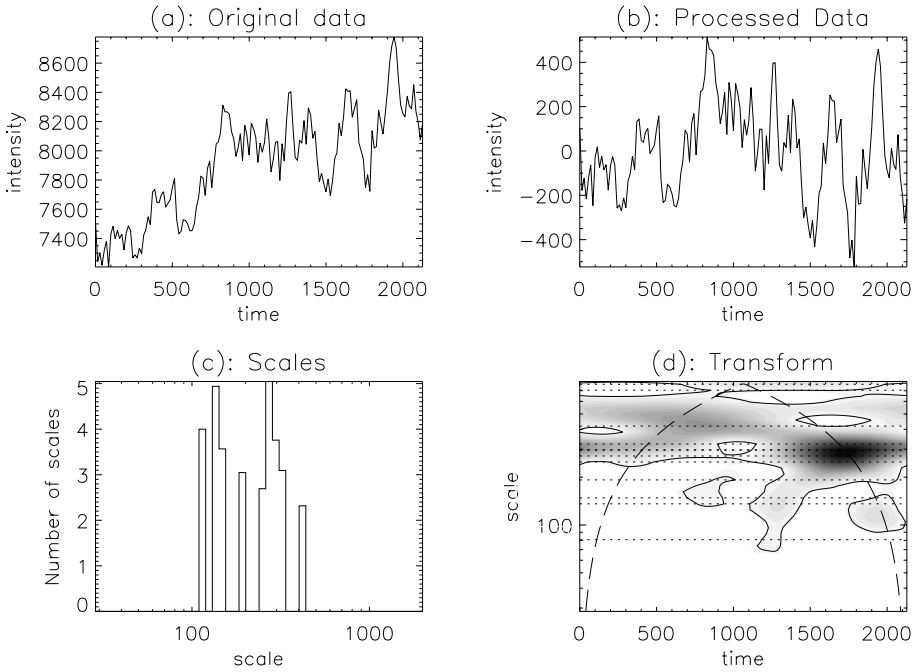

Fig. 4a–d. Counting wave packets in the wavelet transform: example data. The original data **a** is a He I intensity time series formed at pixel 28–31 in file s5763. For details of the wavelet scale counting process see Sect. 3.5.

noise, which for N counts is $\sqrt{N}$. The second is due to the fluctuation in the amplification of the detector system, estimated to be $\sqrt{N}$ and Poisson distributed. These two errors add as the sum of squares, leading to a fractional error $f_N = \sqrt{2/N}$. The quantity S is the fitted signal in the data; hence the term $(f_N S)^2$ describes the contribution to error in I due to the photon statistics.

A time series is formed by summing four consecutive pixels along the solar Y direction; this takes account of the pixel crosstalk in CDS-NIS as described in Thompson (1998). Hence each LOOPS_3 run provides 17 time series formed by summing four consecutive pixels and one of 3 pixels. Single spikes in the time series are smoothed out by taking the average of neighbouring points.

We have already pointed out that the slit is essentially one-dimensional, in the solar Y direction only. In the LOOPS_3 study, a feature is chosen and the slit pointed. Since solar tracking is not present in this study, new material is sliding into the field of view (from the east) as the original material is sliding out (to the west). Hence any time series generated from LOOPS_3 data is a combination of the new material moving in, old material moving out, and the inherent variation of the material in view.

One could ask - why not do some sort of solar tracking to combat this problem? One need only move the slit across the surface of the Sun as it rotates, to keep the same material in view. However, it is not possible to do this perfectly with CDS. The solar tracking capabilities of CDS are as follows. Once a feature is chosen, the instrument keeps the same pointing until the feature has moved two arcseconds. The instrument is then repointed to catch up with the rotated material. For the slit we use, this implies that by the time the repointing is done, the slit will be looking at half new and half old material. So even when solar tracking is switched on, the resultant time series still suffers from the same problem of moving material.

3.2. Wavelet transform

In Sect. 3.1, it was pointed out that new material moves into the field of view of the LOOPS_3 window, and hence the time series is a combination of new material moving into the field of view and the time variability of the material itself. This implies that later parts of the time series refer to different pieces of material that may or may not be magnetically linked to material earlier in the time series. This introduces the idea that any periods in the time series may be strongly localised in time. Hence the method of analysis should take account of this.

Methods such as Fast Fourier Transform and Lomb - Scargle periodogram (Scargle 1982, Horne & Baliunas 1986, Koen 1990) calculate power at particular frequencies by examining the entire time series at the same time and hence, in our dataset, implicitly assume that the material in view remains the same.

Hence power detected at any period in a LOOPS_3 may be due to new material moving into the field of view and not due to the inherent time variability of the plasma, which is the quantity we are more interested in.

However, the localised nature of time series analysis by wavelets makes them ideal for time series generated from LOOPS_3 data, and any other time series suffering from the same problems. Since wavelets are localised in time, when we analyse using wavelets, we sample the time series locally, removing the effect of looking over the entire observation and hence removing the effect of new material moving into the LOOPS_3 field of view.

Let us assume we have a time series of N observations x_n with sample interval δt; then the continuous wavelet transform

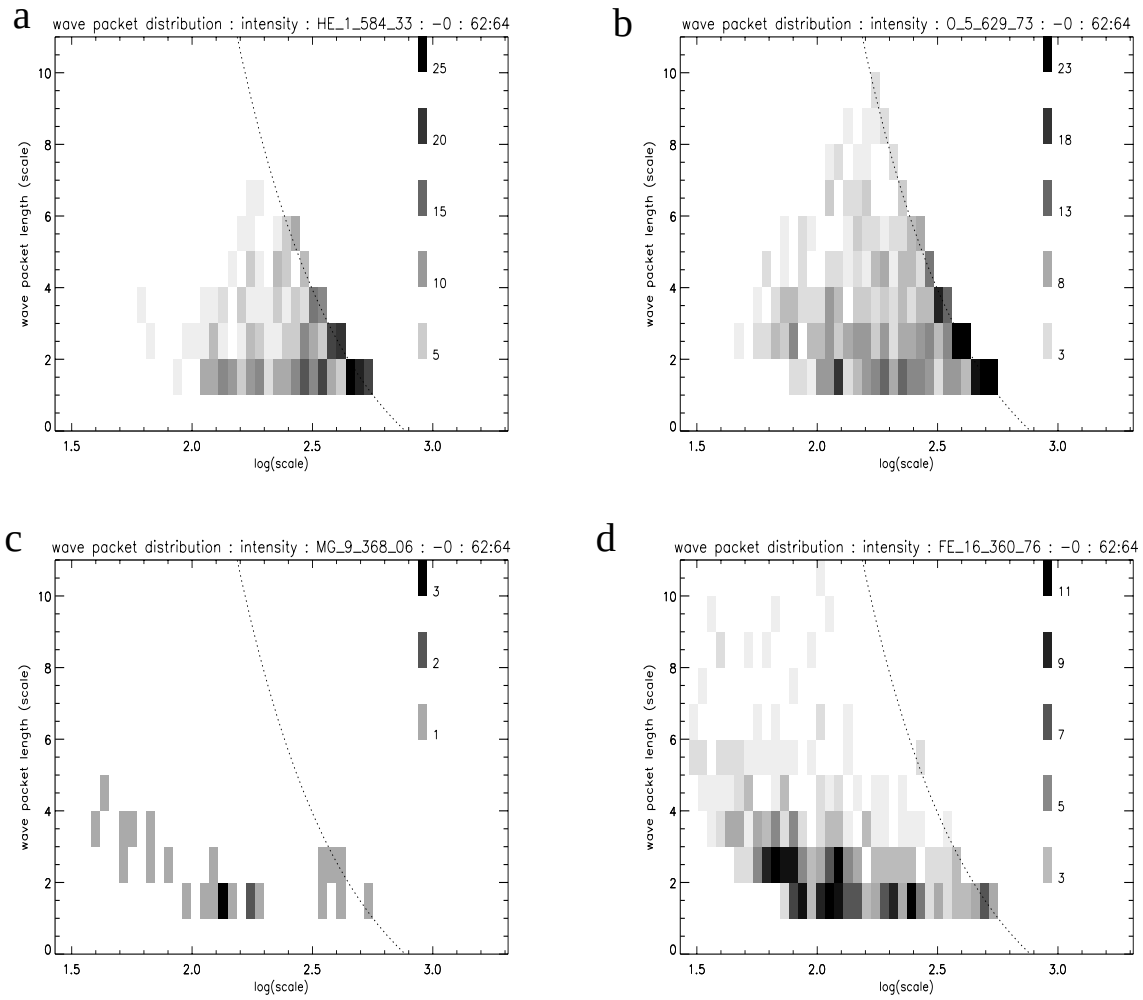

Fig. 5a–d. Frequency distribution of wave packet length as a function of wavelet scale for **a** He I, **b** O V, **c** Mg IX and **d** Fe XVI. Darker rectangles correspond to more frequently found wave packet lengths. The dashed line indicates the maximum length possible for a wave packet at a given scale.

of the time series x_n is defined as the convolution of x_n with an analysing (or mother) wavelet $\psi(\eta)$. We assume that ψ is normalised, i.e., $\int_{\infty}^{\infty} \psi\psi^* d\eta = 1$

For $\eta = (n' - n)\delta t/s$ we have

$$W_n(s) = \sum_{n'=0}^{N-1} x_{n'} \sqrt{\frac{\delta t}{s}} \psi^* \left[\frac{(n' - n)\delta t}{s} \right], \quad (4)$$

where s is the wavelet scale and n allows us to translate the analysing wavelet in time. By varying s and n we can build up a picture of any features in the time series as a function of the analysing scale s and time, as represented by n.

In this paper we use the Morlet wavelet

$$\psi(\eta) = \pi^{-1/4} \exp(i6\eta) \exp\left(-\frac{\eta^2}{2}\right) \quad (5)$$

as our analysing wavelet (Farge 1992). This choice reflects the both the oscillatory and transitory nature of the motions we are looking for and the way the observations were made. We expect any signal to switch on and off and also be affected by material moving in and out of the observing slit.

The wavelet power spectrum is defined as $|W_n(s)|^2$; ranging through n and s allows one to build up a two dimensional transform of the original time series, in scale s and n, the time index.

The wavelet transform also suffers from edge effects at both ends of the time series. This results in a 'cone of influence' in the final transform. Fig. 4d shows a wavelet transform with the cone of influence indicated as a dashed line. Portions of the transform outside the area formed by the time axis and the cone are subject to edge effects.

3.3. Modelling the time series

The choice of model was largely guided by examining the time series. Typically, oscillations are present on top of some linearly varying background. Therefore we choose

$$x_n = a + bt_n + \sum_{n=1}^{N} \sum_{j=1}^{J} A_{n,j} \psi(\eta_{n,j}) + Z_n \quad (6)$$

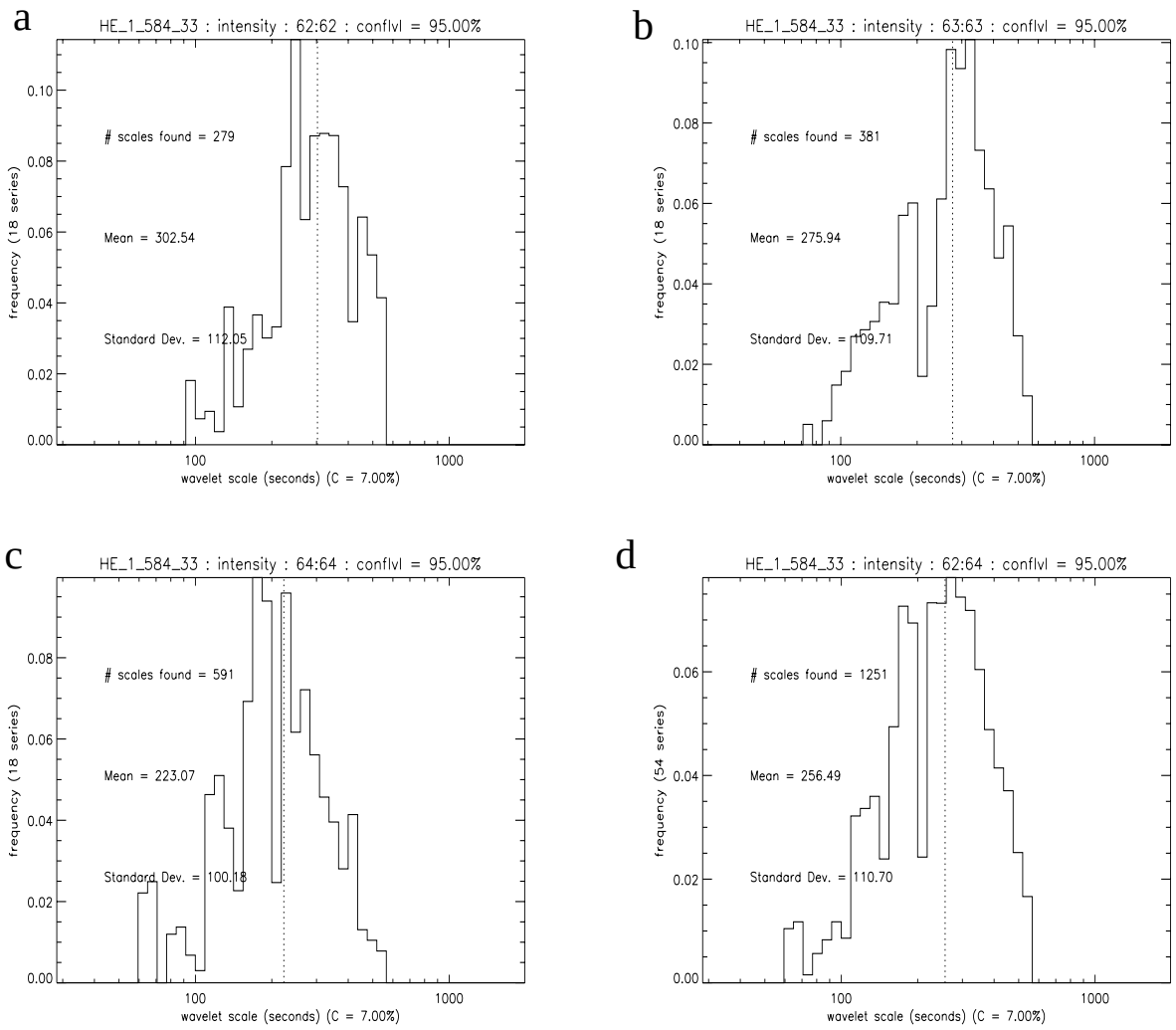

Fig. 6a–d. Frequency distribution of wavelet scales found in He I at location **a** 62, **b** 63 and **c** 64. The cumulative frequency distribution (adding **a**, **b** and **c**) is shown in **d**. The mean is indicated by the dotted vertical line. The value of C was found empirically by examining a number of time series consisting of purely Poisson distributed noise (variances equal to those measured from data) plus one spike and varying C until the relevant scales were completely removed from the transform.

i.e., the sum of a linear trend, a superposition of wavelets and noise Z_n where $\eta_{n,j} = (n' - n)\delta t/s_j$. In the analysis, we subtract a least squares fitted linear polynomial before calculating the wavelet transform.

We determine the significant areas in the wavelet transform by comparing the wavelet transform with that expected by our model for the noise. Any signal significantly greater than that expected from noise is treated as a candidate wave packet signal (see Sect. 3.5). The noise in the data is assumed to be Poisson distributed. Now,

$$|W_n(s)|^2 = N\,|\hat{x}_n(s)|^2 \tag{7}$$

where $\hat{x}_k = \frac{1}{N}\sum_{n=1}^{N-1} x_n \exp(-2i\pi kn/N)$ i.e., the Fourier transform of the original data (Torrence & Compo 1998). Let us assume that x_n is purely Poisson distributed; then from Leahy et al., (1983),

$$|\hat{x}_n(s)|^2 = N_{ph}/N^2 \tag{8}$$

implying that

$$|W_n(s)|^2 = N_{ph}/N.$$

The right hand side can be identified as the variance σ^2 in the original data, assuming that that data is purely Poisson distributed. However we know that in CDS-NIS we cannot simply take N_{ph}/N as the noise present in CDS-NIS observations. Instead we define $\sigma^2_{\rm CDS}$ as the expectation value of the wavelet transform of purely noisy time series as seen in CDS-NIS, i.e.,

$$|W_n(s)|^2 \equiv \sigma^2_{\rm CDS} \tag{9}$$

Eq. 2 defines the noise at each pixel in a LOOPS_3 observation. Since we bin four pixels to produce one time series the σ_I^2 values add at each observation time. The value of $\sigma^2_{\rm CDS}$ is found by averaging these summed values over the number of observations in the time series. This generates an average value to the noise over the time series.

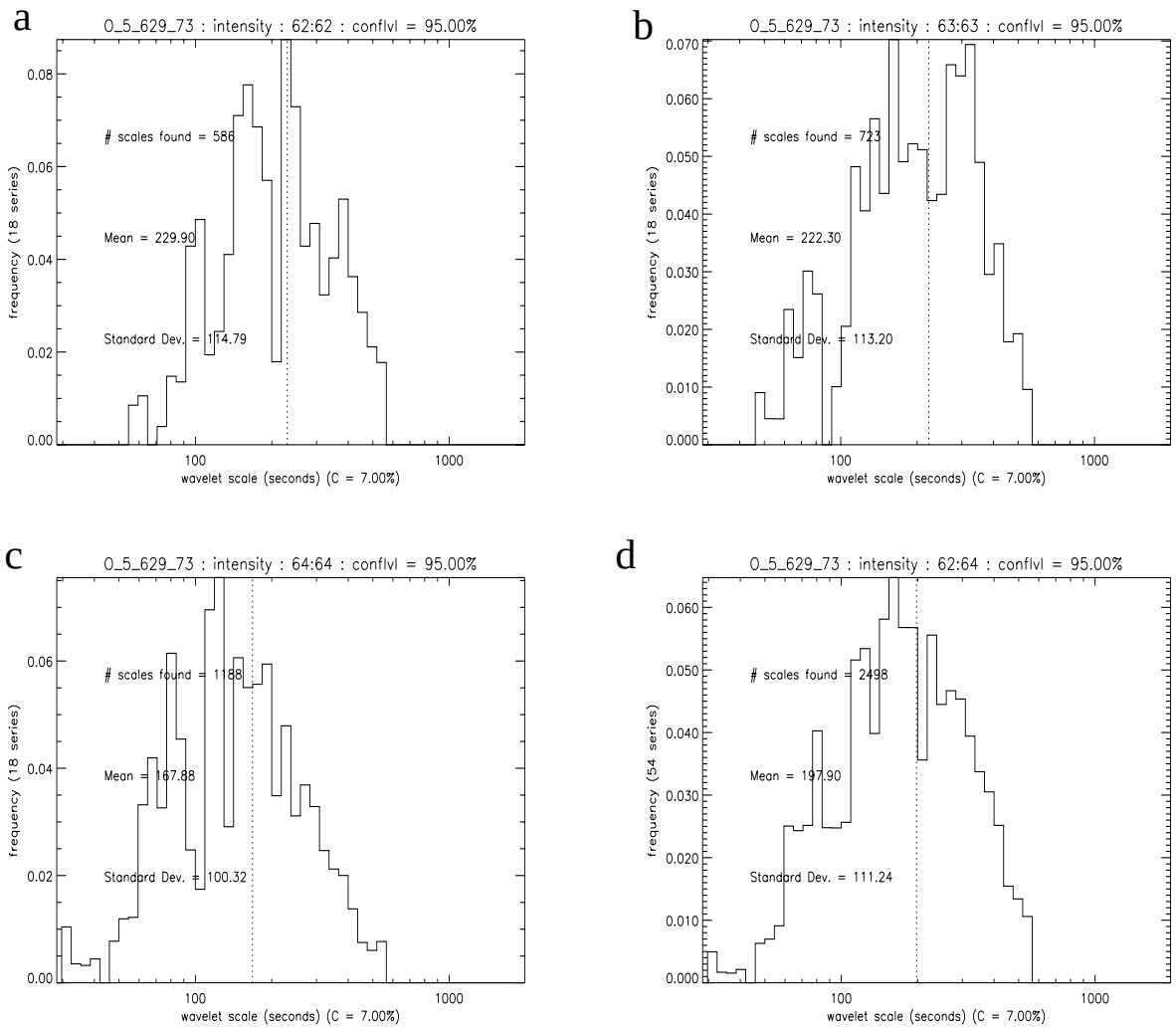

Fig. 7a–d. Frequency distribution of wavelet scales found in O V at location **a** 62, **b** 63 and **c** 64. The cumulative frequency distribution (adding **a**, **b** and **c**) is shown in **d**. The mean is indicated by the dotted vertical line.

From Torrence & Compo (1998), the local wavelet power spectrum is therefore

$$\frac{|W_n|^2}{\sigma^2_{\rm CDS}} \text{is distributed as} \frac{\chi^2_2}{2} \tag{10}$$

at each time n and each scale s, where χ^2_2 is the χ^2 distribution with two degrees of freedom.

To determine, say, the 95% confidence level (significant at 5%) one substitutes the value of χ^2_2 at the 95th percentile. This allows one to calculate 95% confidence contour levels in the wavelet transform $|W_n(s)|^2$ such as those seen in Fig. 4d (solid line). All the results shown here are based on a 95% confidence level.

3.4. Generation of regularly spaced time series

Fig. 2 shows that consecutive sample times are not significantly different from one another. Hence the time series is not significantly unevenly sampled.

We can generate an evenly spaced time series suitable for our wavelet algorithm (see Sect. 3.2) from the original time series by interpolation. The start and end points of the time series remain fixed. A linear polynomial $y = mt + c$ is then found for the i'th pair of points in the irregularly spaced time series (y_{i+1}, t_{i+1}) and (y_i, t_i), where $y \equiv$ data, $t \equiv$ time, $m_i = (y_{i+1} - y_i)/(t_{i+1} - t_i)$ and $c_i = y_{i+1} - m_i t_{i+1}$. The interpolated data Y_i is calculated at new sample times $T_i = t_0 + i.\delta t$ ($\delta t = (t_{N-1} - t_0)/N$) using $Y_i = m_i T_i + c_i$.

Fig. 3 shows an example of the effect of this interpolation process. Plotted are the original time series and the interpolated one. They differ noticeably at only very few points - this is expected given the small difference - less than or on of the order of the square root of the total number of counts - between consecutive sample intervals. For the purposes of this paper this error may be ignored and we may use a regularly spaced wavelet analysis algorithm. Interpolation of irregularly sampled time series to generate a regularly sampled time series has been successfully applied to the wavelet analysis of sunspot groups (Frick et al. 1997).

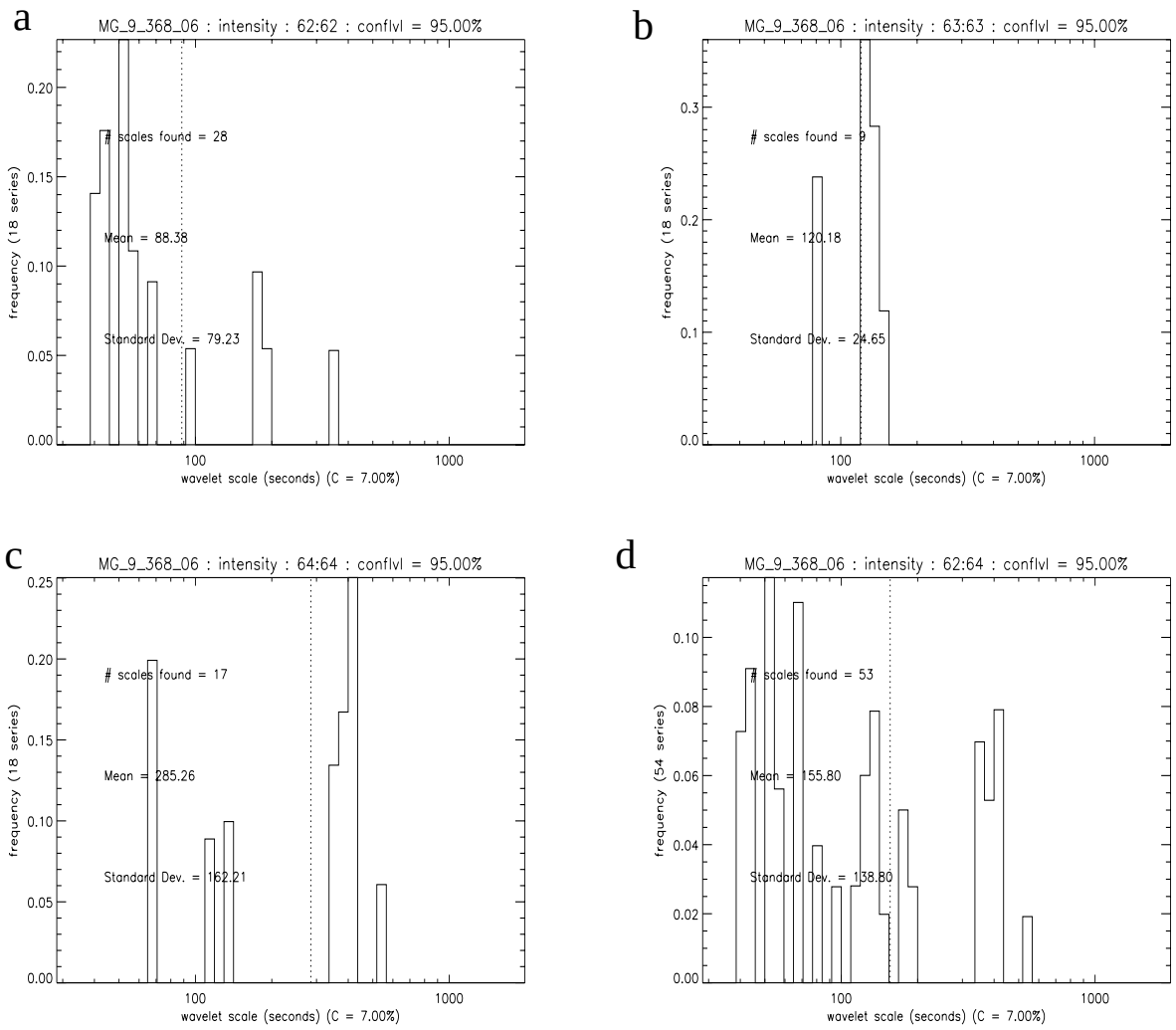

Fig. 8a–d. Frequency distribution of wavelet scales found in Mg IX at location **a** 62, **b** 63 and **c** 64. The cumulative frequency distribution (adding **a**, **b** and **c**) is shown in **d**. The mean is indicated by the dotted vertical line.

3.5. Counting wave packets in the wavelet transform

Fig. 4 shows the process of finding wave packets given a time series that rejects the null hypothesis. The original data (Fig. 4a, a He I intensity time series formed at pixels 28–31 in file s5763) has a linear polynomial subtracted from it and has any spikes removed to form Fig. 4b. Fig. 4c presents the wave packets found and their duration (as a multiple of wavelet scale) in the wavelet transform (Fig. 4d).

Darker regions in (Fig. 4d correspond to regions of higher wavelet power. Also outlined is the 95% confidence contour (solid dark line) in the transform and the cone of influence (dashed line). Clearly, the wavelet transform presents us with a lot of information from which we must sift through to get the scales of the wave packets present in the data. Firstly we discard portions of the transform below the chosen confidence level. Secondly, we also disregard all wavelet power outside the cone of influence. The routine then finds all the local maxima in the remaining portions of the transform. Typically, there are one or two wavelet scales at which significant power exists. At each of these scales (indicated by dotted lines), the duration of the wavelet packet (inside the cone of influence and above the significance level) is measured. The duration of this signal must satisfy two criteria. Firstly, the duration must be greater than or equal to the wavelet scale at which it occurs. This ensures that we have at least one complete oscillation in the wave packet. Secondly, the wave packet duration must be greater than C% of the width of the cone of influence at that wavelet scale. This suppresses the identification of spikes in the data as true wavelet power.

4. Results

4.1. The region observed

The results presented below were obtained from data taken on the 15th November 1996 of an active region present in the south-east quadrant of the Sun. An EJECT_V3 run was taken to start the sequence. This was followed by nine LOOPS_3 runs in three blocks of three. The first block (stored as CDS FITS files labelled s5762r00,01,02) was positioned over a region of positive

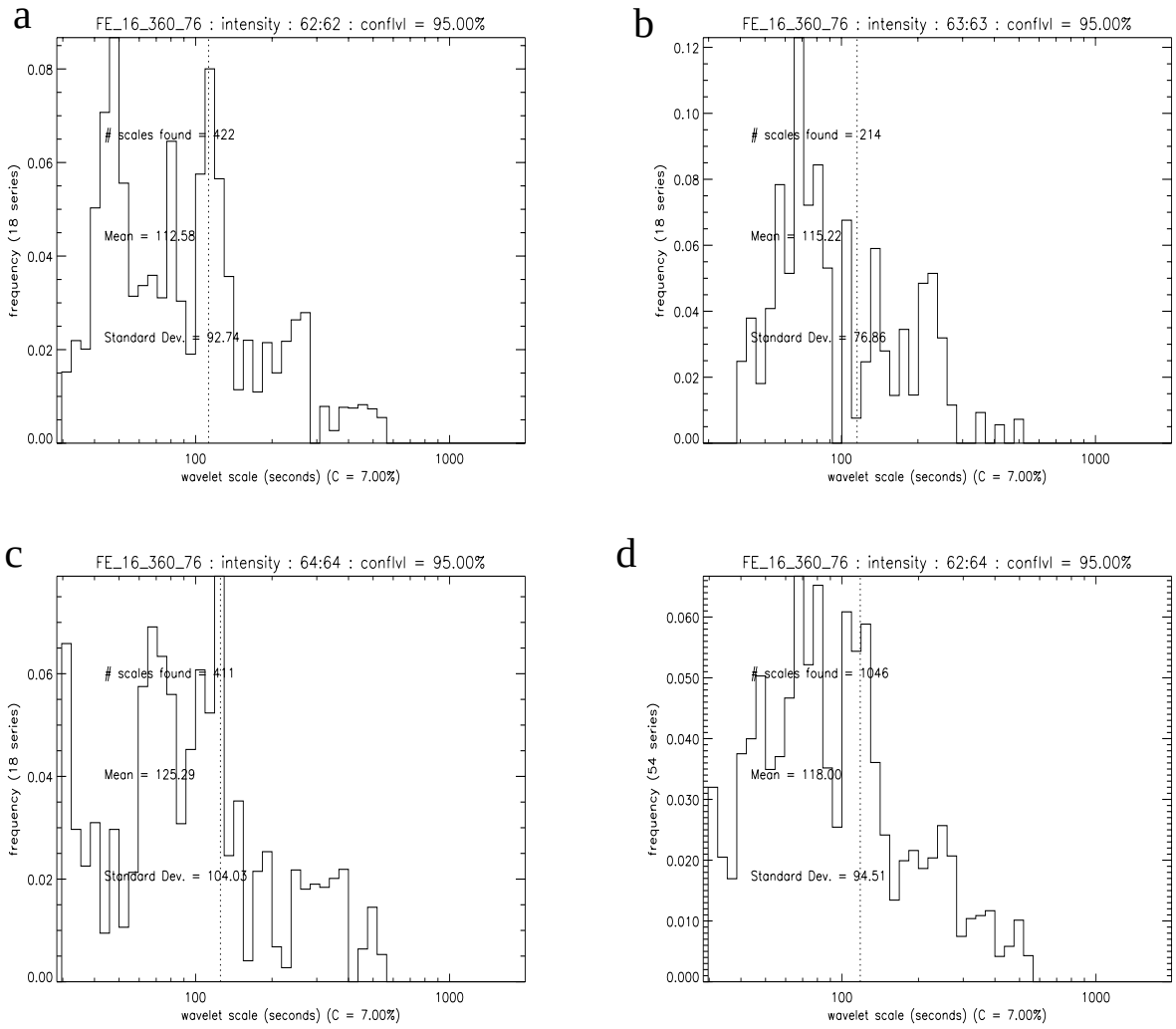

Fig. 9a–d. Frequency distribution of wavelet scales found in Fe XVI at location **a** 62, **b** 63 and **c** 64. The cumulative frequency distribution (adding **a**, **b** and **c**) is shown in **d**. The mean is indicated by the dotted vertical line.

magnetic flux, as observed with the Michelson Doppler Interferometer (MDI) on board SoHO. Similarly, the third block (CDS FITS s5764r00,01,02) of LOOPS_3 runs was placed over the corresponding negative magnetic flux region. The intermediate block was placed between the flux regions (CDS FITS s5763r00,01,02). Each block of three LOOPS_3 runs forms a long duration, high cadence set of observations over physically different parts of an active region. Fig. 1 shows the slit positions over the emerging active region with an instrumental pointing error of ± 5 arcsecs.

4.2. Wavelet scales in the data

Fig. 5 displays histograms of wave packet length found in the data. The plots show how frequently a particular wave packet length is at a given wavelet scale. Darker rectangles correspond to more frequently chosen wave packet lengths at particular wavelet scales. Each plot is formed in the following manner. Having identified a wave packet in the data at a particular scale (according to the criteria laid down in Sect. 3.5), the duration of the wave packet is measured in units of the scale it occurs at. Hence if the wave packet is 780 seconds long at scale 300 seconds then the wave packet is 2.6 scales long, i.e., between 2 and 3 wavelet scales long, and is binned accordingly in the histogram.

He I has a large number of long wavelet scale (greater than 300 seconds) wave packets between one and 3 wavelet scales long. At shorter scales, longer wave packets are detected, though less frequently. Note there are relatively few observations of significant wavelet power at scales less than 100 seconds. O V also shows this same basic pattern, although it is noticeable that there are some observations of significant scales lasting the maximum possible length for a wave packet at that scale. There are also more wave packets found with scales less than 100 seconds in O V when compared to He I.

These distributions are markedly different from those seen in Mg IX and Fe XVI. Virtually no significant wavelet power is found in the Mg IX time series (Fig. 5c and Fig. 8). The wave packet length distribution in Fe XVI is very different from the lower temperature lines. Fe XVI shows a large proportion of

short duration, short (less than 100 seconds) time scale wave packets. Note also that there are numerous examples of long duration (greater than six wavelet scales), short timescale (less than 100 seconds) wave packets in the Fe XVI time series.

Figs. 6-9 show the frequency distribution of the scales found regardless of the wave packet length (as long as the wave packet length is greater than the wavelet scale) at position 62, 63, and 64 (see Fig. 1) and the cumulative distribution (a, b, c and d respectively).

These figures are formed in a similar manner to Figs. 5a–d: instead of binning wave packet lengths into integer bins and noting how many of each we find, we add up all the fractional lengths at a particular scale. Hence Figs. 6d, 7d, 8d and 9d roughly correspond to the distribution found by summing Fig. 5 along the y axis.

Figs. 6a–c are basically single peaked distributions of similar widths but different means. The joint distribution Fig. 6d has a broad peak with many scales found within one standard deviation of the peak, about 170 to 350 seconds, i.e., 2.8–5.8 mHz. This lies in the range found by White & Athay (1979a) Athay & White (1979a), Athay & White (1979b) and White & Athay (1979b) (2.5–9 mHz) and overlaps with the range 2–5 mHz found by Doyle et al., (1997). Figs. 6b is strongly peaked around 300 seconds while Figs. 6a and 6c are peaked closer to 200 seconds, lending the overall distribution a broad peak.

The transition region line results (Fig. 7) also show evidence of a 300 second oscillation, particularly Fig. 7b. Note that all three distributions 7(a), (b) and (c) show large numbers of oscillations at around 160–200 seconds. Doyle et al., (1998) report on quiet sun oscillations in the upper transition region and note the presence of power at 5 mHz which would correspond to the peak in the distribution Fig. 7d.

In comparison with the other lines, there are virtually no statistically significant wavelet scales found in Mg IX (Fig. 8). This implies that oscillations are either not present at all or that if oscillations are present then they are not resolved by the instrument, given the noise in the data and the spatial and temporal resolutions.

However, significant numbers of scales are found in Fe XVI. Figs. 9a–c all have approximately the same mean: however the distributions look rather incomplete when compared to their cumulation in Fig. 9d, and even here the distribution is patchy. The mode of this distribution is around 60–70 seconds, with large numbers of wave packets found at even shorter wavelet scales. This is borne out if we look to Fig. 5d where there are examples of long duration wave packets at short wavelet scales. These short timescales are not without precedent in the corona; McKenzie & Mullan (1997) observe periods in the range 9.6–61.6 seconds in Yohkoh SXT (Soft X-ray Telescope) images of active region loops.

Fig. 9a has two large peaks at 48s and 113s. The shorter period of these two observations is close to the 43 s found by Koutchmy et al., (1983) in Doppler velocity oscillations of Fe XIV 5303 Å coronal line and 43 s in intensity found by Rušin & Minarovjech (1994) in an analysis of the red and green coronal lines. A period of 112s was also detected by Rušin & Minarovjech (1994). There are some longer wavelet scales also present in the data above 300 seconds, which coincide approximately with periods found by Egan & Schneeberger (1979) (360s, line width) and Tsubaki (1977) (320s, Dopler velocity) in Sacramento Peak Observatory Fe XIV active region coronal emission line spectra.

5. Discussion

We have tried to pick out only the most interesting scales in the wavelet transform by limiting our search to statistically interesting areas of sufficient duration inside the cone of influence. For the length of dataset in this paper the longest scale that could satisfy our criteria is about 550 seconds. A longer dataset, however, would increase this upper limit.

There are several wave packets at a number of scales, especially in He I and O V that lie on the maximum detectable length for the length of this time series. Clearly longer time series are needed to establish upper limits to the duration of wave packets in the solar atmosphere.

The localised nature of the wavelet transform allows us to obviate the problem of material moving in and out of the field of view. It is also this localisation that allows one to measure the duration of wave packets in the data. The results suggest that detectable oscillations last in the solar atmosphere for only a few timescales, implying that either the source of the oscillations exists for only a few timescales or that the waves are damped with a few timescales.

This information is important for many wave heating theories as the wave must survive long enough for the mechanism to provide sufficient heating, e.g., resonant absorption. Poedts et al., (1990) shows that the linear cylindrical loop model considered requires 140 driving periods (50 s period) - corresponding to about 2 hours - to reach a steady state. Poedts & Boynton (1996) shows that in nonlinear magnetohydrodynamic simulations of footpoint driven coronal loops about 30 driving periods were required before the loop absorbed over 80% of the incident energy. These numerical studies suggest that wave packets must be relatively long to support resonant absorption. The current data set does not contain any evidence of wave packets lasting that long. However, note that Wright & Rickard (1995) point out that loops driven by a broadband spectrum of frequencies can also be efficiently heated by Alfvén resonant absorption, subject to two conditions, namely that either the fast or global eigenfrequencies of the loop must lie within the spectrum of the driver and that the fast eigenfrequencies must lie in the Alfvén continuum.

The results also suggest that each temperature may have a particular wavelet scale distribution. The chromospheric and transition region lines He I and O V have peaked distributions suggesting a preferred timescale at these temperatures.

The low coronal Mg IX shows very few scales above the confidence level, suggesting that the variations in intensity are mostly random at this temperature, given the spatial and temporal resolution of CDS-NIS.

Yet the higher temperature Fe XVI shows evidence of being peaked, this time at a scale far less than observed in the lower temperature lines. This suggests that the source of the wave packets in the corona are very different from those in the chromosphere and transition region. This may be indicative of different oscillation mechanisms acting at different temperatures. These distributions - of both wave packet length and wavelet scale - available through such a wavelet analysis, can help characterise the behaviour of the solar atmosphere.

Acknowledgements. RWW was funded for this work by a PPARC Research Fellowship. JI was funded through an ESA External Fellowship and PPARC. All would like to acknowledge the encouragement and friendliness of all those present at the Experimental Operations and Analysis Facilities at the Goddard Space Flight Centre, Greenbelt, Maryland, USA. Wavelet software was provided by C. Torrence and G. Compo, and is available at URL: http://paos.colorado.edu/research/wavelets/. Thanks also to Dr. G. W. Inverarity, Dr. A. J. C. Belien and Dr. A. Fludra for many useful discussions on time series analysis.

References

Aschwanden M.J., Kliem B., Schwarz U., et al., Kurths J., 1998, ApJ 505, 941
Athay R.G., White O.R., 1979a, ApJS 39, 333
Athay R.G., White O.R., 1979b, ApJ 229, 1147
Bocchialini K., Baudin F., 1994, A&A 299, 893
Browning P.K., 1991, Plasma Physics and controlled nuclear fusion 33, 6, 539
Chapman R.D., Jordan S.D., Neupert W.M., Thomas R.J., 1972, ApJ 174, L97
Davila J.M., 1987, ApJ 317, 514
Doyle J.G., van den Oord G.H.J., O'Shea E., 1997, A&A 327, 365
Doyle J.G., van den Oord G.H.J., O'Shea E., Banerjee D., 1998, Sol. Phys. 181, 51
Edwin P.M., 1991, Ann. Geophysicae 9, 188
Egan T.F., Schneeberger T.J., 1979, Sol. Phys. 64, 223
Farge M., 1992, Ann. Rev. Fluid Mech. 24, 395
Frick P., Galyagin D., Hoyt D.V., et al., 1997, A&A 328, 670
Harrison R.A., Sawyer E.C., Carter M.K., et al., 1995, Sol. Phys. 163, 233
Heyvaerts J., Priest E.R., 1983, A&A 117, 220
Heyvaerts J., Priest E.R., 1992, ApJ 390, 297
Hollweg J.V, 1987, 312, 880
Hollweg J.V, 1990, Computer Physics Reports 12, 205
Hood A. W., Gonzalez-Delgado D.G., Ireland J., 1997, A&A 324, 11
Horne J.H., Baliunas S.L., 1986, ApJ 302, 757
Ionson J.A., 1978, ApJ 226, 650
Ireland J., 1996, Ann. Geophysicae 14, 485
Kappraff J.M., Tataronis J.A., 1977, J. Plasma Phys. 18 (2), 209
Karpen J.T., Dahlburg R.B., Davila J.M., 1994, ApJ 421, 372
Koen C., 1990, ApJ 348, 700
Koutchmy S., Žugžda Y.D., Locăns V., 1983, A&A 120, 185
Laing G.B., Edwin P.M., 1995, Sol. Phys. 157, 103
Leahy D.A., Darbro W., Elsner R.F., et al., 1983, ApJ 266, 160
McKenzie D.E., Mullan D.J., 1997, Sol. Phys. 176, 127
Narain U., Ulmschneider P., 1990, Space Sci. Rev. 54, 377
Parker E.N., 1988, ApJ 330, 474
Poedts S., Boynton G.C., 1996, A&A 306, 610
Poedts S., Goossens M., Kerner W., 1990, Comput. Physics. Comm. 59, 95
Poedts S., Kerner W., 1992, J. Plasma Phys. 47 (1), 139
Porter L.J., Klimchuk J.A., Sturrock P.A., 1994a, ApJ 435, 482
Porter L.J., Klimchuk J.A., Sturrock P.A., 1994b, ApJ 435, 502
Roberts B., Edwin P.M., Benz A.O., 1984, ApJ 279, 857
Rušin V., Minarovjech M., 1994, In: Rušin V., Heinzel P., Vial J.-C. (eds.) IAU Colloquim 144 Solar Coronal Structures. 487
Ruderman M.S., Goossens M., 1993, Sol. Phys. 143, 69
Scargle J.D., 1982, ApJ 263, 835
Švestka Z., 1994, Sol. Phys. 152, 505
Thompson W.T., 1998, CDS Software Note No. 49, available from CDS homepage at http://orpheus.nascom.nasa.gov/cds/home/software_notes.html
Torrence C., Compo G.P., 1998, Bull. Amer. Meteor. Soc. 79, 61
Tsubaki T., 1977, Sol. Phys. 51, 121
Ulrich R.K., 1996, ApJ 465, 436
White O.R., Athay R.G., 1979a, ApJS 39, 317
White O.R., Athay R.G., 1979b, ApJS 39, 347
Wright A.N., Rickard G.J., 1995, ApJ 444, 458
Zirker J.B., 1993, Sol. Phys. 148, 43